

Plasmonic polarons induced by alkali-atom deposition in hafnium disulfide ($1T$ -HfS₂)

Christoph Emeis,¹ Sanjoy Kr Mahatha,^{2,3} Sebastian Rohlf,⁴ Kai Rossnagel,^{3,4,5} and Fabio Caruso^{1,5}

¹*Institut für Theoretische Physik und Astrophysik, Kiel University, 24098 Kiel, Germany*

²*UGC-DAE Consortium for Scientific Research, University Campus, Khandwa Road, Indore - 452001, India*

³*Ruprecht-Haensel-Labor, Deutsches Elektronen-Synchrotron DESY, 22607 Hamburg, Germany*

⁴*Institut für Experimentelle und Angewandte Physik, Kiel University, 24098 Kiel, Germany*

⁵*Kiel Nano, Surface and Interface Science KiNSIS, 24118 Kiel, Germany*

(Dated: July 12, 2023)

We combine ab-initio calculations based on many-body perturbation theory and the cumulant expansion with angle-resolved photoemission spectroscopy (ARPES) to quantify the electron-plasmon interaction in the highly-doped semiconducting transition metal dichalcogenide $1T$ -HfS₂. ARPES reveals the emergence of satellite spectral features in the vicinity of quasiparticle excitations at the bottom of the conduction band, suggesting coupling to bosonic excitations with a characteristic energy of 200 meV. Our first-principles calculations of the photoemission spectral function reveal that these features can be ascribed to electronic coupling to carrier plasmons (doping-induced collective charge-density fluctuations). We further show that reduced screening at the surface enhances the electron-plasmon interaction and is primarily responsible for the emergence of plasmonic polarons.

I. INTRODUCTION

The existence of satellite structures in the spectral function of solids has been known since the infancy of photoemission spectroscopy [1]. Satellites have first been identified by X-ray photoemission spectroscopy (XPS) in elemental metals – such as Al [1, 2], alkali (Li, Na) [3], and alkaline earth metals (Be, Mg) [4] – as broadened replica of the valence and core density of states red-shifted by multiples of the plasmon energy. Besides ordinary metals, photoemission satellites have been observed in pristine semiconductors (as, e.g., undoped silicon [5]) – where the excitation of photoholes couples to valence plasmons. Ab-initio calculations and angle-resolved photoemission experiments later revealed that full band-structure replicas can arise from the simultaneous excitations of a photohole and a valence plasmon [6–8].

The interest in photoemission satellites has been revived by the discovery of photoemission satellites due to the Fröhlich electron-phonon interactions in highly-doped anatase TiO₂ [9], and in the 2D electron gas formed at the surface of SrTiO₃ [10]. These features have been recognized as the smoking-gun evidence for the formation of Fröhlich polarons – strongly-coupled quasiparticles resulting from the dressing of photoexcited holes by polar longitudinal optical phonons [11, 12]. Overall, the emergence of satellite structures in photoemission spectroscopy is a hallmark of strong electron-boson interaction in solids, and it has provided a strong stimulus for the development of new ab-initio theories for electron-boson coupling, including Fröhlich coupling [13–15], density-functional [16–18] and many-body polaron theories [11, 19], electron-plasmon interaction [20], and the cumulant expansion approach [5–7, 21–25].

At variance with metals and pristine semiconductors, satellites in highly-doped semiconductors and insulators occur in the immediate vicinity of the band edges, and thus influence fundamental properties of direct rel-

evance for the transport and dynamics of charge carriers, including quasiparticle lifetimes and effective masses [26, 27]. Changes of the doping concentration can further be exploited to exert control on the electron-phonon and electron-plasmon coupling strength, with visible effects on the structure of photoemission satellites [28]. In particular, doping-induced free carriers can screen the electron-phonon interaction, suppressing the formation of Fröhlich polarons and washing out the corresponding spectral fingerprints in ARPES [9, 14]. At the same time, at large doping concentrations carrier plasmons can be excited in materials, with plasmon energies and electron-plasmon coupling strengths that increase with the carrier density. At strong coupling, electron-plasmon interactions can result in the formation of plasmonic polarons with spectral signatures analogous to those of phonon-induced polaronic satellites [28–30].

Plasmonic polarons have thus far only been observed in a handful of materials, including EuO [28], anatase TiO₂ [29], and monolayer MoS₂ [30]. A challenge that must be overcome for the observation of these phenomena consists in reaching the very high doping concentrations (of the order of $n = 10^{20} \text{ cm}^{-3}$) – which are required for the emergence of an electron liquid while preserving the sample crystallinity. In EuO, these conditions have been realized via Eu-substitution by Gd [28]; in anatase, TiO₂ free carriers are introduced by oxygen vacancies [29]; highly-doped MoS₂ monolayers have been realized by stimulating the formation of chalcogen vacancies via thermal annealing [30].

In this work, we realize strong electron-plasmon interactions via the deposition of alkali atoms on the surface of hafnium disulfide ($1T$ -HfS₂). To corroborate this new way of controlling the electron-plasmon interaction, we conduct a combined theoretical and experimental investigation of the electronic and quasiparticle excitations for pristine and highly-doped $1T$ -HfS₂. ARPES measurements for n -doped samples reveal the emergence of satellite spectral structures in the vicinity of the quasi-

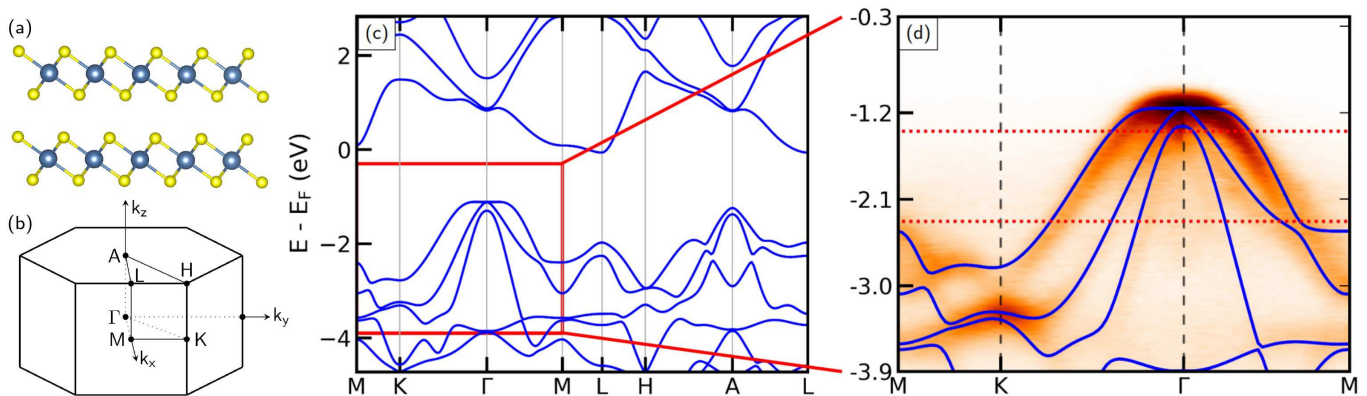


FIG. 1. (a) Crystal structure of 1T-HfS₂ (side view) and (b) corresponding hexagonal Brillouin zone. (c) DFT band structure of pristine bulk 1T-HfS₂. Energies are relative to the conduction band minimum. (d) DFT band structure superimposed on the ARPES spectral function for energies and crystal momenta within the red rectangle in panel (c). Dark (light) colors denote high (low) values of the spectral function. The dashed red lines mark the energies of the ARPES intensity maps of Fig. 2(a)-2(b).

particle peak at the bottom of the conduction band. To unravel the origin of these features we performed ab-initio calculations of the electron spectral function by explicitly including the influence of electron-plasmon interaction in the Fan-Migdal approximation. Spectral function calculations based on the cumulant expansion approach – the state of the art for the description of satellites in photoemission – are in excellent agreement with ARPES experiments, corroborating the plasmonic origin of the ARPES satellites. These findings demonstrate that alkali doping in bulk transition metal dichalcogenides can alter the spectrum of quasiparticle excitations, providing a viable route to realize strong electron-plasmon coupling.

The manuscript is structured as follows. In Sec. II experimental and computational methods are discussed. In Sec. III, we present ARPES measurements and ab-initio calculations of pristine 1T-HfS₂. In Sec. IV we discuss the theory and measurements of plasmonic polarons in the ARPES spectral function of highly-doped 1T-HfS₂. Concluding remarks are presented in Sec. V.

II. METHOD

1T-HfS₂ single crystals were grown by chemical vapor transport at the in-house facilities. The sample was cleaved inside the ultra-high vacuum chamber at room temperature and subsequently transferred to the liquid helium-cooled manipulator for photoemission measurements. During the ARPES measurements, the sample temperature was maintained at 10 K. *In situ* doping of the 1T-HfS₂ samples was achieved by depositing potassium atoms from an alkali metal dispenser (SAES Getters) on the surface. The dopant atoms adsorbed on the surface and sub-surface, but did not intercalate into deeper layers of the van der Waals material.

The experiments were performed at beamline P04 of PETRA III at DESY using the ASPHERE photoelectron

spectroscopy endstation. The area probed by the synchrotron beam had a size of approximately $15 \times 15 \mu\text{m}^2$, the photon energies used and corresponding total energy resolution of the ARPES measurements were within a range of 260-450 eV and 50-80 meV, respectively. The Fermi surface map of the doped 1T-HfS₂ sample in Fig. 2 was recorded at a photon energy of 432 eV, probing the 11th Γ point in the k_z direction.

Density functional theory (DFT) calculations were performed with the plane-wave pseudopotential code Quantum ESPRESSO [31]. We used the Perdew-Burke-Ernzerhof (PBE) generalized gradient approximation for the exchange-correlation functional [32] and Optimized Norm-Conserving Vanderbilt fully relativistic pseudopotentials [33]. The plane-wave kinetic energy cutoff was set to 120 Ry and the integrals over the Brillouin zone were discretized on a $12 \times 12 \times 6$ Monkhorst-Pack k -point mesh. Spin-orbit coupling (SOC) was included at all steps of our calculations. The band structure was interpolated onto a $60 \times 60 \times 30$ homogeneous grid via maximally-localized Wannier functions [34] as implemented in the WANNIER90 package [35]. The effect of n -type doping was included by rigidly shifting the Fermi level above the conduction-band bottom to account for additional free carriers. Charge neutrality of the system is retained by introducing a compensating positively charged homogeneous background. Ab-initio calculations of the electron-plasmon interaction were conducted with the EPW code [36] and employed the Fan-Migdal approximation for the electron self-energy and the cumulant expansion for the spectral function [5, 37].

III. ELECTRONIC PROPERTIES OF PRISTINE 1T-HfS₂

1T-HfS₂ crystallizes in a layered crystal structure with a hexagonal unit cell belonging to the 164 space group

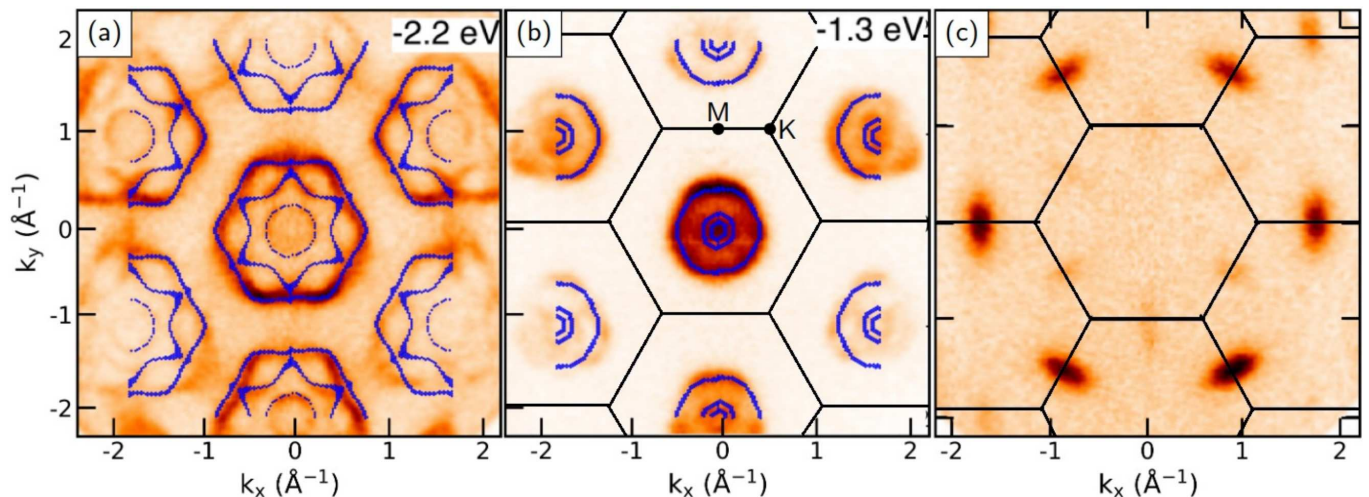


FIG. 2. ARPES intensity distributions in the k_x - k_y -plane taken at -2.2 eV (a) and -1.3 eV (b) relative to the conduction band minimum for pristine 1T-HfS₂. The DFT bands are marked in blue. Black hexagons mark the boundaries of the Brillouin zone with the Γ point in the centre. The position of the M and K high-symmetry points is marked in panel (b). (c) ARPES intensity map taken at the Fermi level of highly-doped 1T-HfS₂. Ellipsoidal intensity patterns reflect the population of the bottom of the conduction band by alkali deposition-induced free-carrier doping. Due to ARPES matrix element effects the intensity of the pockets in the first Brillouin zone is suppressed.

($P\bar{3}m1$). A side view of the 1T-HfS₂ crystal structure and its Brillouin zone are shown in Fig. 1(a) and 1(b), respectively. The bulk band structure of pristine 1T-HfS₂ as obtained from DFT-PBE is shown in Fig. 1(c). The path across the Brillouin zone passes through the M-K- Γ -M and the L-H-A-L high-symmetry points and it was chosen to facilitate comparison with the ARPES measurements. 1T-HfS₂ is an indirect band gap semiconductor with the valence band maximum (conduction band minimum) located at the Γ (L) high-symmetry point. The calculated indirect band gap of 1.2 eV is in good agreement with earlier DFT studies [38, 39]. Analysis of the projected DOS (not shown) reveals that the valence bands arise primarily from the hybridization of p -orbitals with S character, while the conduction bands are predominantly characterized by the d -orbitals with Hf character [40]. In heavy elements with unfilled 5d orbitals, such as Hf, SOC has important effects on the electronic structure [41]. In 1T-HfS₂ it leads to a shift of the valence band maximum to Γ and induces a bandsplitting of the two highest valence bands, while the conduction band minimum remains unaffected. The influence of SOC on the band structure is further discussed in Appendix A.

A parabolic fitting to the conduction-band minimum along the three reciprocal lattice vectors yields the following values for the electron effective masses $m_1^* = 0.25 m_e$, $m_2^* = 1.65 m_e$, and $m_3^* = 0.20 m_e$, which are in good agreement with earlier DFT calculations [42]. The density of states (DOS) effective mass was determined as $m_{\text{DOS}}^* = (gm_1^*m_2^*m_3^*)^{3/2}$, where $g = 6$ is the degeneracy factor of the conduction band minimum, yielding $m_{\text{DOS}}^* = 1.44 m_e$ [43].

The measured ARPES spectral function for the valence band along the M-K- Γ -M high-symmetry path is

shown in Fig. 1(d). The DFT-PBE band structure, superimposed on the measurements for comparison, is in very good agreement with the experiments. We observe a small deviation between measurements and calculations in the vicinity of the K high-symmetry point for energies around -3.0 eV, which we tentatively attribute to the finite k_z broadening, resulting in the superposition of ARPES intensities corresponding to different k_z -planes of the Brillouin zone.

In Figs. 2(a) and 2(b) we show the measured ARPES intensity maps for crystal momenta spanning the k_x - k_y -plane for energies corresponding to -2.2 eV and -1.3 eV below the Fermi energy marked by horizontal dashed lines in Fig. 1(d), respectively. The ab-initio band structure evaluated from DFT and interpolated using maximally-localized Wannier functions closely matches the experimental data within the first Brillouin zone. The slight deviations in the second Brillouin zones are attributed to the k_z variation of constant-energy ARPES angle maps.

IV. POLARONS IN HIGHLY-DOPED 1T-HfS₂

In the following we investigate the influence of n -type doping on the band structure and on the spectrum of quasiparticle excitations of 1T-HfS₂. Figure 2(c) shows the ARPES measurement of the Fermi surface of highly-doped 1T-HfS₂. While no signal is seen at these energies for the pristine sample, finite intensity arises from the population of the conduction band due to doping. The elliptical intensity pattern reflects the anisotropic band dispersion of the lowest conduction band. Due to photoe-

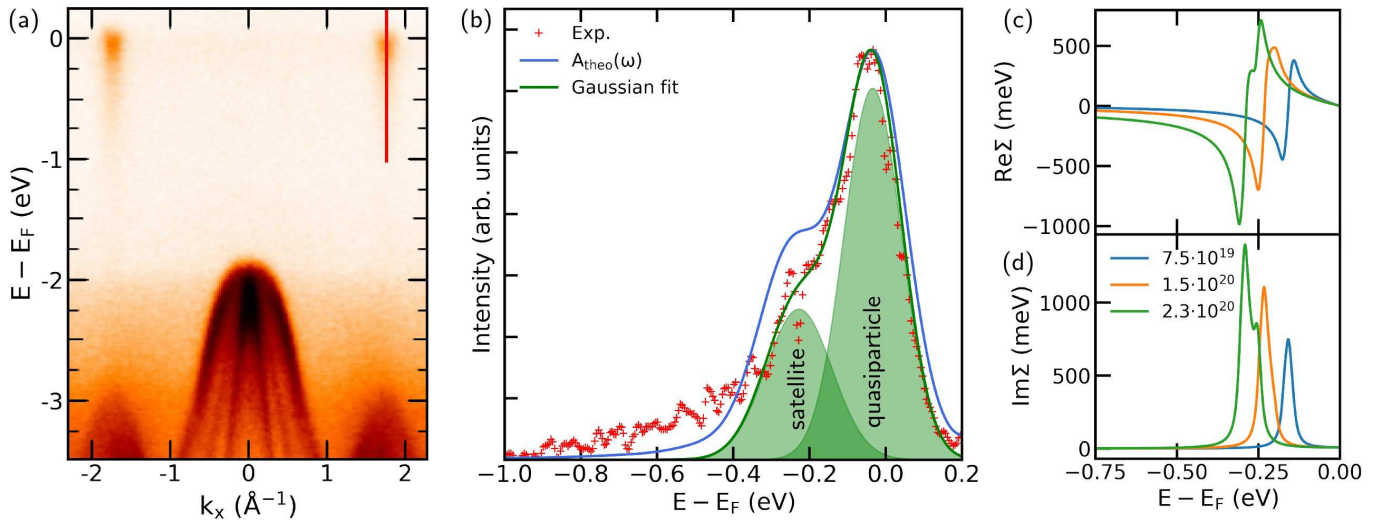


FIG. 3. (a) ARPES measurements of highly-doped 1T-HfS₂ with a charge carrier concentration of $n = 1.5 \cdot 10^{20} \text{ cm}^{-3}$. ARPES intensity map around the Fermi level reflecting the population of the conduction-band bottom and exhibiting a polaronic tail extending down to -1 eV below the conduction band edge. (b) ARPES spectrum (red crosses) and *ab-initio* spectral function (blue line) in the vicinity of the conduction-band bottom for energies and momentum marked by the red line in panel (a). A Shirley background was subtracted from the experimental data. The spectral function calculations are based on cumulant expansions and broadened by a Gaussian with a variance of 80 meV to match the experimental resolution. Two Gaussians (green shading) illustrate the decomposition of the total ARPES intensity into a quasiparticle peak and a satellite peak. (c)-(d) Real and imaginary parts of the electron self-energies due to electron-plasmon interaction for different carrier concentrations given in cm^{-3} .

mission matrix element effects, the intensity in the first Brillouin zone is suppressed. The extrinsic carrier concentration of $n = 1.5 \cdot 10^{20} \text{ cm}^{-3}$ is extracted from the size of the Fermi pockets of Fig. 2(c).

The extrinsic charge carriers introduced by *n*-type dopants can significantly modify the electronic properties [44, 45]. In addition to the population of the conduction-band bottom, the doping-induced extrinsic carriers can lead to the emergence of carrier plasmons with a characteristic frequency given by $\omega_{\text{pl}} = \sqrt{4\pi n e^2 / m_{\text{DOS}}^* \epsilon_{\infty}}$, with high-frequency dielectric constant ϵ_{∞} and DOS effective mass m_{DOS}^* [46]. In doped semiconductors, the plasmon energy can span values between 10 and 200 meV [20]. These low-energy plasmons can further couple to carriers in the conduction band via electron-plasmon interactions leading to the emergence of polaronic quasiparticle excitations [28–30, 47]. In the following, we proceed to investigate these phenomena on a quantitative ground, by combining *ab-initio* theory and ARPES measurements of highly-doped 1T-HfS₂.

The band structure of the *n*-doped 1T-HfS₂ obtained by ARPES along Γ -K-M direction is shown in Fig. 3(a). The energies are relative to the Fermi level, which is located 50 meV above the conduction-band bottom. Compared to the pristine sample, structural disorder and additional doping-induced scattering processes contribute to an enhancement of the band structure broadening. For photoelectron energies above the fundamental gap (1.9 eV), our measurements reveal the emergence of additional photoemission intensities that reflect the

population of the conduction-band bottom by the alkali deposition-induced carriers. The Fermi pockets of the conduction band are centered around $|k_x| = 1.8 \text{ \AA}^{-1}$. Figure 3(b) illustrates the ARPES spectral function $A_{\text{exp}}(\omega)$ for energies and crystal momentum marked by the red line in Fig. 3(a). In Fig. 3(b), we eliminated the background signal from the experimental data by subtracting a Shirley background function $B(\omega)$, defined as $B(\omega) = \beta \int_{\omega}^{\mu} d\omega' I(\omega')$ where β is an adjustable parameter and μ is the chemical potential [48]. The resulting spectral function $A_{\text{exp}}(\omega)$ is characterized by a sharp quasiparticle peak and an additional shoulder structure at 200 meV below the Fermi level, with a decreasing photoemission intensity extending down to 1 eV below the Fermi level. A Gaussian decomposition of the ARPES intensity, marked in green in Fig. 3(b), suggests that these spectral features are compatible with a superposition of a quasiparticle peak and a photoemission satellite peak red-shifted by 200 meV from the maximum of the quasiparticle peak.

The emergence of photoemission satellites in doped semiconductors is a hallmark of strong electron-boson interaction which has been widely investigated in the past owing to its close relation to the formation of Fröhlich polarons – a prototypical emergent phenomenon due to strong electron-phonon coupling. The energy separation between quasiparticle and satellite peaks is expected to match the energy of the boson that underpins the coupling. For example, Fröhlich polarons in polar semiconductors arise from the coupling of *n*-type carriers with

polar longitudinal-optical (LO) phonons, and they manifest themselves in ARPES spectra via satellite structures at energies matching the LO phonon energies. In 1*T*-HfS₂, the energy separation between the quasiparticle and satellite peak (200 meV) exceeds the LO phonon energies (<40 meV, see e.g., the phonon dispersion in Appendix B). The discrepancy of these energy scales enables us to promptly exclude the Fröhlich electron-phonon interaction as a source of polaronic coupling. The absence of spectral fingerprints of Fröhlich polarons can be easily rationalized by noting that (i) 1*T*-HfS₂ is a weakly polar crystal, i.e., it is characterized by small Born effective charges, and (ii) at the high doping concentration considered in our work electron-phonon coupling is screened by free carriers, thus, further mitigating the effects of Fröhlich coupling.

In the following, we thus proceed to inspect the electron-plasmon interaction as a possible source of polaronic coupling, and we analyze its influence on the emergence of photoemission satellites. To quantify the electron-plasmon interaction and its effect on the ARPES measurements, we evaluate the electron self-energy due to the electron-plasmon interaction, which in the Fan-Migdal approximation can be expressed as [20]:

$$\Sigma_{n\mathbf{k}}^{\text{epl}} = \int \frac{d\mathbf{q}}{\Omega_{\text{BZ}}} \sum_m |g_{mn}^{\text{epl}}(\mathbf{k}, \mathbf{q})|^2 \quad (1)$$

$$\times \left[\frac{n_{\mathbf{q}} + f_{m\mathbf{k}+\mathbf{q}}}{\varepsilon_{n\mathbf{k}} - \varepsilon_{m\mathbf{k}+\mathbf{q}} + \hbar\omega_{\mathbf{q}}^{\text{pl}} + i\eta} + \frac{n_{\mathbf{q}} + 1 - f_{m\mathbf{k}+\mathbf{q}}}{\varepsilon_{n\mathbf{k}} - \varepsilon_{m\mathbf{k}+\mathbf{q}} - \hbar\omega_{\mathbf{q}}^{\text{pl}} + i\eta} \right]$$

where Ω_{BZ} is the Brillouin zone volume, m and n are band indices, \mathbf{k} and \mathbf{q} are Bloch wave vectors, $n_{\mathbf{q}}$ denotes the Bose-Einstein and $f_{m\mathbf{k}+\mathbf{q}}$ the Fermi-Dirac distribution, ε are the Kohn-Sham (KS) eigenstates, $\omega_{\mathbf{q}}^{\text{pl}}$ is the plasmon frequency and η is a positive infinitesimal. The integral runs over the Brillouin zone volume. The first term accounts for electron scattering processes involving the absorption of a plasmon $+\omega_{\mathbf{q}}^{\text{pl}}$, while the second term accounts for hole scattering processes mediated by plasmon emission. g_{mn}^{epl} denotes the electron-plasmon coupling matrix elements, that can be expressed as [20]:

$$g_{mn}^{\text{epl}}(\mathbf{k}, \mathbf{q}) = \left[\frac{\partial \varepsilon(\mathbf{q}, \omega)}{\partial \omega} \Big|_{\omega_{\mathbf{q}}^{\text{pl}}} \right]^{-\frac{1}{2}} \quad (2)$$

$$\times \left(\frac{4\pi}{\Omega_{\text{BZ}}} \right)^{\frac{1}{2}} \frac{1}{|\mathbf{q}|} \langle \psi_{m\mathbf{k}+\mathbf{q}} | e i \mathbf{q} \cdot \mathbf{r} | \psi_{n\mathbf{k}} \rangle.$$

Here, ε is the dielectric function, $\langle \psi_{m\mathbf{k}+\mathbf{q}} | e i \mathbf{q} \cdot \mathbf{r} | \psi_{n\mathbf{k}} \rangle$ the dipole matrix element and $\psi_{\mathbf{k}}$ the Kohn-Sham orbital. The $|\mathbf{q}|^{-1}$ singularity in the electron-plasmon coupling matrix element is reminiscent of the Fröhlich interaction in polar semiconductors, and it indicates that the long-wavelength plasmons dominate electron-plasmon scattering processes.

Owing to the dependence of the matrix elements g_{mn}^{epl} on the dielectric function, the electron-plasmon inter-

action is profoundly influenced by the screening environment of the system. In 1*T*-HfS₂, the alkali dopant atoms are concentrated in the vicinity of the surface and, possibly, underneath the first 1*T*-HfS₂ layers of the sample. Correspondingly, the dielectric screening experienced by *n*-type carriers is mitigated as compared to bulk carriers. To account for the charge localization at the surface we introduce an effective dielectric constant $\varepsilon_{\infty}^{\text{S}} = (\varepsilon_{\infty}^{\text{HfS}_2} + 1)/2 = 3.6$, with $\varepsilon_{\infty}^{\text{HfS}_2} = 6.2$ being the high-frequency dielectric constant of bulk 1*T*-HfS₂ [49, 50]. Further details on the evaluation of the electron-plasmon matrix elements can be found elsewhere [47]. Based on this value, we estimate the plasmon frequency to be 200 meV for a doping concentration $n = 1.5 \cdot 10^{20} \text{ cm}^{-3}$, which matches closely the satellite energy, thus, suggesting electron-plasmon coupling as a likely origin of this polaronic feature.

In Figs. 3(c)-(d) the real and imaginary part of the electron self-energy due to electron-plasmon coupling are presented, respectively, for doping carrier concentrations $n = 7.5 \cdot 10^{19}$, $1.5 \cdot 10^{20}$, and $2.25 \cdot 10^{20} \text{ cm}^{-3}$. The middle value coincides with the doping concentration determined from experiment. The corresponding imaginary parts of the self-energy in Fig. 3(d) exhibit a sharply peaked structure with a Lorentzian line profile in the vicinity of the energy $\varepsilon_{\mathbf{k}} - \hbar\omega_{\text{pl}}$. For larger doping concentrations, we observe a progressive red-shift of the peak in $\text{Im}\Sigma$ and an increase of its intensity, which arise from the increase of plasmon energy and of the electron-plasmon coupling matrix elements, respectively. The real part of the self-energy is related to $\text{Im}\Sigma$ by a Kramers-Kronig's transformation and it thus also has a similar dependence on the doping concentration.

Based on the electron self-energy, we proceed to investigate the signatures of electron-plasmon coupling in ARPES. Earlier studies revealed that ab-initio calculations of photoemission satellites based on the Fan-Migdal approximation overestimate the satellite energy and intensity by up to 50% as compared to experiment [5, 25]. To circumvent this limitation, we evaluate the spectral function based on the cumulant expansion approach [5]. The cumulant expansion representation of the spectral function can be expressed as [22, 25, 51]:

$$A(\mathbf{k}, \omega) = \sum_n e^{A_{n\mathbf{k}}^{\text{S}1}(\omega)} * A_{n\mathbf{k}}^{\text{QP}}(\omega). \quad (3)$$

Here, $*$ denotes a convolution product and $A_{n\mathbf{k}}^{\text{QP}}(\omega) = 2\pi^{-1} \text{Im}[\hbar\omega - \varepsilon_{n\mathbf{k}} - \Sigma_{n\mathbf{k}}^{\text{epl}}(\varepsilon_{n\mathbf{k}})]^{-1}$ is the quasiparticle contribution to the spectral function evaluated in the ‘‘on the energy shell’’ approximation, in which the frequency dependence of the self-energy $\Sigma_{n\mathbf{k}}(\omega)$ is replaced by the KS energy $\omega = \varepsilon_{n\mathbf{k}}$ [52, 53]. The satellite part of spectral function is further given by [47]:

$$A_{n\mathbf{k}}^{\text{S}1}(\omega) = - \frac{\beta_{n\mathbf{k}}(\omega) - \beta_{n\mathbf{k}}(\varepsilon_{n\mathbf{k}}) - (\omega - \varepsilon_{n\mathbf{k}})\beta'_{n\mathbf{k}}(\varepsilon_{n\mathbf{k}})}{(\omega - \varepsilon_{n\mathbf{k}})^2}, \quad (4)$$

with $\beta = \pi^{-1} \text{Im} \Sigma_{nk}(\varepsilon_{nk} - \omega)\Theta(\omega)$ and β' denoting its first derivative. The first term in the Taylor series expansion of the exponential in Eq. (3) corresponds to the quasiparticle peak of the photoemission spectrum, while higher-order terms account for plasmon-assisted scattering up to infinite order. In the following, we truncated Eq. (3) to the second order. Terms above the second order contribute negligibly to the spectral function and their inclusion is inconsequential.

The spectral function in the vicinity of the conduction-band bottom computed from Eqs. (3)-(4) is shown in Fig. 3(b). To account for the finite experimental resolution, the spectral function has been convoluted with a Gaussian with a variance of 80 meV. The intensity of the convoluted spectral function is rescaled to match the experimental spectrum at the quasiparticle peak. Experimental broadening and intensity rescaling are the only adjustable parameters in our simulations. In short, the cumulant spectral function exhibits a pronounced shoulder arising from the convolution of the satellite and quasiparticle spectral function $A^S * A^{QP}$. This spectral feature corresponds to the coupled excitation of a photo-hole and a plasmon and matches closely the photoemission satellite measured in ARPES. Higher-order satellite structures due to multiple plasmon excitations have small intensity and they are washed out by the finite experimental resolution. Overall, the close agreement between simulations and measurements suggest that carrier plasmons in highly-doped 1T-HfS₂ are strongly coupled to free carriers in the conduction bands, leading to the formation of plasmonic polarons and to corresponding spectral fingerprints in the ARPES spectrum. The residual discrepancy between theory and experiments at energies smaller than -0.5 eV is tentatively attributed to impurity scattering and statistical noise, which are not captured by the Shirley background model.

V. CONCLUSION

In summary, we conducted ab-initio calculations and ARPES measurements of the electronic properties and quasiparticle excitation of pristine and highly-doped 1T-HfS₂. We report the observation of polaronic satellites in the ARPES spectral function, which we attribute to the formation of plasmonic polarons. Our first-principles calculations of the Fan-Migdal self-energy for electron-plasmon interaction explicitly account for extrinsic carriers introduced by alkali doping and closely reproduce the spectral fingerprints of polaronic satellites in the measured ARPES spectral function. In particular, the alkali doping enables the injection of free carriers in the vicinity of the surface, where screening is weak and it thus provides ideal conditions for realizing strong coupling between free carriers and plasmons.

Overall, our combined theoretical and experimental investigation reveals the possibility to tailor quasiparticle excitations and the electron-plasmon coupling strength

via extrinsic doping mediated by the adsorption and intercalation of alkali atoms affecting the first atomic layers of 1T-HfS₂.

Materials interfaces and hybrid heterostructures may provide further opportunities to directly control the dielectric environment and, thus, tailor the spectrum of quasiparticle interactions.

ACKNOWLEDGMENTS

This work was funded by the Deutsche Forschungsgemeinschaft (DFG), Projects No. 499426961 and 434434223 – SFB 1461. We thank DESY (Hamburg, Germany), a member of the Helmholtz Association HGF, for the provision of experimental facilities. Parts of this research were performed at PETRA III. Funding for the photoemission spectroscopy instrument at beamline P04 (contracts 05KS7FK2, 05K10FK1, 05K12FK1, and 05K13FK1 with Kiel University; 05KS7WW1 and 05K10WW2 with the University of Würzburg) by the German Federal Ministry of Education and Research (BMBF) is gratefully acknowledged.

APPENDIX A: INFLUENCE OF SPIN-ORBIT COUPLING ON THE BAND STRUCTURE

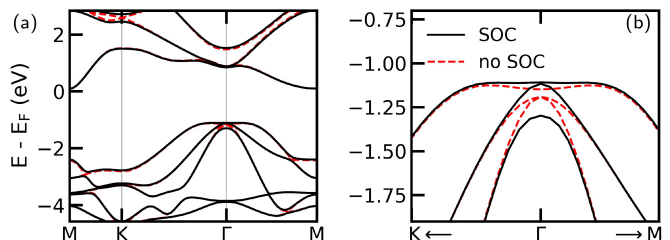


FIG. 4. Electronic band structure of 1T-HfS₂ calculated using DFT with and without SOC.

In Fig. 4 the band structure of 1T-HfS₂ with (black, continuous) and without (red, dashed) SOC is depicted. SOC leads to an avoided crossing in both the valence and conduction bands, lifting the degeneracy of upper valence bands at the Γ point. These findings are in good agreement with earlier calculations [41].

APPENDIX B: PHONON DISPERSION

In Fig. 5 the phonon dispersion of 1T-HfS₂ obtained from density functional perturbation theory (DFPT) is presented. The discontinuity of the second and third highest-energy modes at the Γ point arises from the LO-TO splitting. The highest phonon mode has a frequency of 43 meV.

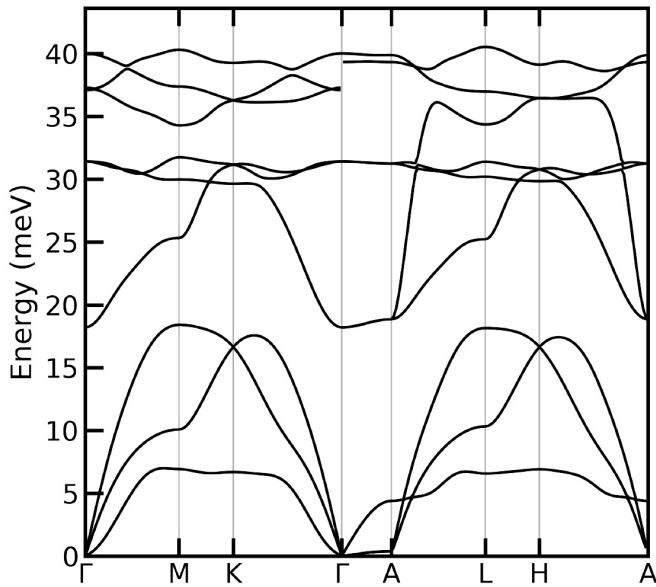


FIG. 5. Phonon dispersion of 1T-HfS₂ calculated using DFPT.

-
- [1] Y. Baer and G. Busch, X-ray photoemission from aluminum, *Phys. Rev. Lett.* **30**, 280 (1973).
- [2] A. Barrie, X-ray photoelectron spectra of aluminium and oxidised aluminium, *Chem. Phys. Lett.* **19**, 109 (1973).
- [3] S. P. Kowalczyk, L. Ley, F. R. McFeely, R. A. Pollak, and D. A. Shirley, X-Ray Photoemission from Sodium and Lithium, *Phys. Rev. B* **8**, 3583 (1973).
- [4] W. J. Pardee, G. D. Mahan, D. E. Eastman, R. A. Pollak, L. Ley, F. R. McFeely, S. P. Kowalczyk, and D. A. Shirley, Analysis of surface- and bulk-plasmon contributions to x-ray photoemission spectra, *Phys. Rev. B* **11**, 3614 (1975).
- [5] M. Guzzo, G. Lani, F. Sottile, P. Romaniello, M. Gatti, J. J. Kas, J. J. Rehr, M. G. Silly, F. Sirotti, and L. Reining, Valence electron photoemission spectrum of semiconductors: Ab initio description of multiple satellites, *Phys. Rev. Lett.* **107**, 166401 (2011).
- [6] F. Caruso, H. Lambert, and F. Giustino, Band structures of plasmonic polarons, *Phys. Rev. Lett.* **114**, 146404 (2015).
- [7] J. Lischner, G. K. Pálsson, D. Vigil-Fowler, S. Nemsak, J. Avila, M. C. Asensio, C. S. Fadley, and S. G. Louie, Satellite band structure in silicon caused by electron-plasmon coupling, *Phys. Rev. B* **91**, 205113 (2015).
- [8] F. Caruso and F. Giustino, Spectral fingerprints of electron-plasmon coupling, *Phys. Rev. B* **92**, 045123 (2015).
- [9] S. Moser, L. Moreschini, J. Jaćimović, O. Barišić, H. Berger, A. Magrez, Y. Chang, K. Kim, A. Bostwick, E. Rotenberg, *et al.*, Tunable polaronic conduction in anatase TiO₂, *Phys. Rev. Lett.* **110**, 196403 (2013).
- [10] Z. Wang, S. McKeown Walker, A. Tamai, Y. Wang, Z. Ristic, F. Y. Bruno, A. De La Torre, S. Riccò, N. C. Plumb, M. Shi, P. Hlawenka, J. Sánchez-Barriga, A. Varykhalov, T. K. Kim, M. Hoesch, P. D. C. King, W. Meevasana, U. Diebold, J. Mesot, B. Moritz, T. P. Devereaux, M. Radovic, and F. Baumberger, Tailoring the nature and strength of electron-phonon interactions in the SrTiO₃(001) 2D electron liquid, *Nat. Mater.* **15**, 835 (2016).
- [11] C. Franchini, M. Reticcioli, M. Setvin, and U. Diebold, Polarons in materials, *Nat. Rev. Mater.* **6**, 560 (2021).
- [12] M. Kang, S. W. Jung, W. J. Shin, Y. Sohn, S. H. Ryu, T. K. Kim, M. Hoesch, and K. S. Kim, Holstein polaron in a valley-degenerate two-dimensional semiconductor, *Nat. Mater.* **17**, 676 (2018).
- [13] C. Verdi and F. Giustino, Fröhlich electron-phonon vertex from first principles, *Phys. Rev. Lett.* **115**, 176401 (2015).
- [14] C. Verdi, F. Caruso, and F. Giustino, Origin of the crossover from polarons to fermi liquids in transition metal oxides, *Nat. Commun.* **8**, 15769 (2017).
- [15] G. Antonius, S. Poncé, E. Lantagne-Hurtubise, G. Aulclair, X. Gonze, and M. Côté, Dynamical and anharmonic effects on the electron-phonon coupling and the zero-point renormalization of the electronic structure, *Phys. Rev. B* **92**, 085137 (2015).
- [16] G. Miceli, W. Chen, I. Reshetnyak, and A. Pasquarello, Nonempirical hybrid functionals for band gaps and polaronic distortions in solids, *Phys. Rev. B* **97**, 121112 (2018).
- [17] W. H. Sio, C. Verdi, S. Poncé, and F. Giustino, Polarons from First Principles, without Supercells, *Phys. Rev. Lett.* **122**, 246403 (2019).
- [18] V. Vasilchenko, A. Zhugayevych, and X. Gonze, Variational polaron equations applied to the anisotropic Fröhlich model, *Phys. Rev. B* **105**, 214301 (2022).
- [19] J. Lafuente-Bartolome, C. Lian, W. H. Sio, I. G. Gurtubay, A. Eiguren, and F. Giustino, Unified Approach to Polarons and Phonon-Induced Band Structure Renor-

- malization, Phys. Rev. Lett. **129**, 076402 (2022).
- [20] F. Caruso and F. Giustino, Theory of electron-plasmon coupling in semiconductors, Phys. Rev. B **94**, 115208 (2016).
- [21] D. C. Langreth, Singularities in the x-ray spectra of metals, Phys. Rev. B **1**, 471 (1970).
- [22] F. Aryasetiawan, L. Hedin, and K. Karlsson, Multiple plasmon satellites in Na and Al spectral functions from ab initio cumulant expansion, Phys. Rev. Lett. **77**, 2268 (1996).
- [23] J. Lischner, D. Vigil-Fowler, and S. G. Louie, Physical origin of satellites in photoemission of doped graphene: An ab initio GW plus cumulant study, Phys. Rev. Lett. **110**, 146801 (2013).
- [24] J. J. Kas, J. J. Rehr, and L. Reining, Cumulant expansion of the retarded one-electron green function, Phys. Rev. B **90**, 085112 (2014).
- [25] F. Caruso, C. Verdi, and F. Giustino, *Many-Body Calculations of Plasmon and Phonon Satellites in Angle-Resolved Photoelectron Spectra Using the Cumulant Expansion Approach* (Springer, 2020) pp. 341–365.
- [26] F. Giustino, Electron-phonon interactions from first principles, Rev. Mod. Phys. **89**, 015003 (2017).
- [27] B. Guster, P. Melo, B. A. A. Martin, V. Brousseau-Couture, J. C. de Abreu, A. Miglio, M. Giantomassi, M. Côté, J. M. Frost, M. J. Verstraete, and X. Gonze, Fröhlich polaron effective mass and localization length in cubic materials: Degenerate and anisotropic electronic bands, Phys. Rev. B **104**, 235123 (2021).
- [28] J. M. Riley, F. Caruso, C. Verdi, L. Duffy, M. D. Watson, L. Bawden, K. Volckaert, G. van der Laan, T. Hesjedal, M. Hoesch, *et al.*, Crossover from lattice to plasmonic polarons of a spin-polarised electron gas in ferromagnetic euo, Nat. Commun. **9**, 1 (2018).
- [29] X. Ma, Z. Cheng, M. Tian, X. Liu, X. Cui, Y. Huang, S. Tan, J. Yang, and B. Wang, Formation of Plasmonic Polarons in Highly Electron-Doped Anatase TiO₂, Nano Lett. **21**, 430 (2021).
- [30] F. Caruso, P. Amsalem, J. Ma, A. Aljarb, T. Schultz, M. Zacharias, V. Tung, N. Koch, and C. Draxl, Two-dimensional plasmonic polarons in n-doped monolayer MoS₂, Phys. Rev. B **103**, 205152 (2021).
- [31] P. Giannozzi, S. Baroni, N. Bonini, M. Calandra, R. Car, C. Cavazzoni, D. Ceresoli, G. L. Chiarotti, M. Cococcioni, I. Dabo, *et al.*, Quantum espresso: a modular and open-source software project for quantum simulations of materials, J. Phys. Condens. Matter **21**, 395502 (2009).
- [32] J. P. Perdew, K. Burke, and M. Ernzerhof, Generalized gradient approximation made simple, Phys. Rev. Lett. **77**, 3865 (1996).
- [33] D. R. Hamann, Optimized norm-conserving vanderbilt pseudopotentials, Phys. Rev. B **88**, 085117 (2013).
- [34] N. Marzari, A. A. Mostofi, J. R. Yates, I. Souza, and D. Vanderbilt, Maximally localized Wannier functions: Theory and applications, Rev. Mod. Phys. **84**, 1419 (2012).
- [35] G. Pizzi, V. Vitale, R. Arita, S. Blügel, F. Freimuth, G. Géranton, M. Gibertini, D. Gresch, C. Johnson, T. Koretsune, *et al.*, Wannier90 as a community code: new features and applications, J. Phys. Condens. Matter **32**, 165902 (2020).
- [36] S. Poncé, E. R. Margine, C. Verdi, and F. Giustino, EPW: Electron-phonon coupling, transport and superconducting properties using maximally localized Wannier functions, Comput. Phys. Commun. **209**, 116 (2016).
- [37] F. Caruso and F. Giustino, The GW plus cumulant method and plasmonic polarons: application to the homogeneous electron gas, Eur. Phys. J. B **89**, 1 (2016).
- [38] K. Iordanidou, M. Houssa, G. Pourtois, V. Afanas'ev, and A. Stesmans, Impact of point defects and oxidation on the electronic properties of HfS₂ monolayers, ECS J. Solid State Sci. Technol. **5**, Q3054 (2016).
- [39] J. Shang, S. Zhang, X. Cheng, Z. Wei, and J. Li, Electric field induced electronic properties modification of ZrS₂/HfS₂ van der Waals heterostructure, RSC Adv. **7**, 14625 (2017).
- [40] S. N. Neal, S. Li, T. Birol, and J. L. Musfeldt, Chemical bonding and born charge in 1T-HfS₂, NPJ 2D Mater. Appl. **5**, 45 (2021).
- [41] K. W. Lau, C. Cocchi, and C. Draxl, Electronic and optical excitations of two-dimensional ZrS₂ and HfS₂ and their heterostructure, Phys. Rev. Mater. **3**, 074001 (2019).
- [42] H. Lu, Y. Guo, and J. Robertson, Band edge states, intrinsic defects, and dopants in monolayer HfS₂ and SnS₂, Appl. Phys. Lett. **112**, 062105 (2018).
- [43] M. A. Green, Intrinsic concentration, effective densities of states, and effective mass in silicon, J. Appl. Phys. **67**, 2944 (1990).
- [44] E. Ziambaras, J. Kleis, E. Schröder, and P. Hyldgaard, Potassium intercalation in graphite: A van der Waals density-functional study, Phys. Rev. B **76**, 155425 (2007).
- [45] K. Rosnagel, Suppression and emergence of charge-density waves at the surfaces of layered 1T – TiSe₂ and 1T – TaS₂ by in situ Rb deposition, New J. Phys. **12**, 125018 (2010).
- [46] G. Giuliani and G. Vignale, *Quantum Theory of the Electron Liquid* (Cambridge University Press, 2005).
- [47] F. Caruso, C. Verdi, S. Poncé, and F. Giustino, Electron-plasmon and electron-phonon satellites in the angle-resolved photoelectron spectra of n-doped anatase TiO₂, Phys. Rev. B **97**, 165113 (2018).
- [48] D. A. Shirley, High-resolution x-ray photoemission spectrum of the valence bands of gold, Phys. Rev. B **5**, 4709 (1972).
- [49] G. Lucovsky, R. White, J. Benda, and J. Revelli, Infrared-reflectance spectra of layered group-IV and group-VI transition-metal dichalcogenides, Phys. Rev. B **7**, 3859 (1973).
- [50] T. Iwasaki, N. Kuroda, and Y. Nishina, Anisotropy of lattice dynamical properties in ZrS₂ and HfS₂, J. Phys. Soc. Japan **51**, 2233 (1982).
- [51] F. Aryasetiawan and O. Gunnarsson, The GW method, Rep. Prog. Phys. **61**, 237 (1998).
- [52] B. Gumhalter, V. Kovač, F. Caruso, H. Lambert, and F. Giustino, On the combined use of GW approximation and cumulant expansion in the calculations of quasiparticle spectra: The paradigm of Si valence bands, Phys. Rev. B **94**, 035103 (2016).
- [53] J. J. Quinn and R. A. Ferrell, Electron self-energy approach to correlation in a degenerate electron gas, Phys. Rev. **112**, 812 (1958).